



Research paper

Large diameter laterally loaded piles in sand: Numerical evaluation of soil stress paths and relevance of laboratory soil element testing

Xiaoyang Cheng^{a,*}, Erdin Ibraim^a, Haoyuan Liu^b, Federico Pisanò^c, Andrea Diambra^a

^a Department of Civil Engineering, University of Bristol, Bristol BS8 1QU, UK

^b Norwegian Geotechnical Institute, Sognsveien 72, Oslo 0806, Norway

^c Faculty of Civil Engineering and Geosciences, Delft Univ. of Technology, 2628 CN, Delft, Netherlands

ARTICLE INFO

Keywords:

Large-diameter pile

Stress path

Monotonic loading

Laboratory element testing

Finite element

ABSTRACT

This paper uses 3D numerical analyses to investigate the stress path experienced by soil elements around large diameter piles in sand subjected to monotonic drained lateral loading. Inspection of the loading-induced stresses in the soil revealed the multiaxial nature of these stress paths, which are characterised by rotation of one or more principal stress axes. Based on the outcome of the finite element analyses, typical stress paths for different soil elements around the piles are extracted. Such stress paths are then evaluated against those enabled by conventional and advanced laboratory soil element testing. It is found that a combination of tests in the Hollow Cylinder Torsional Apparatus (HCTA) can reproduce most features of the numerically identified stress paths for soil elements around the pile. Unavoidable limitations in laboratory testing are discussed as well as the major challenge in replicating the loading direction with respect to the material axes. Some guidance for the experimental implementation of these stress paths in the HCTA are provided as well as a discussion on the use of conventional experimental equipment, such as the conventional triaxial or simple shear apparatus.

1. Introduction

The experimental characterisation of soils through the use of laboratory element testing is crucial for any robust geotechnical system design process. Advanced design procedures benefit from laboratory tests which eventually mimic stress paths experienced by critical soil elements around geotechnical systems. The prediction of a geotechnical structure response invariably relies on accurate mechanical soil characterisation which must be appropriately embedded (i.e. through constitutive modelling) in analytical and/or numerical methods.

The growth of offshore renewable energy systems in the last decade has considerably driven the engineering and design optimisation of large diameter monopiles, which have been the selected foundation option for about 80% of the installed offshore wind turbine projects (Ramirez et al., 2020). To produce more wind power, the offshore wind market is progressively considering larger turbines in deeper water sites, currently requiring extremely large sized monopiles with diameter in excess of 10 m for wind turbines up to 14–15 MW capacity. While the challenges associated with the manufacturing, storage, transportation and installation of foundations of this size (note that pile length can easily exceed 100 m considering both the soil embedded and underwater sections) have cost project implications, any optimisation

of the foundation design should reduce these costs including mitigation of project risks. Currently, 3D finite element (FE) analyses are typically employed in the design of large diameter monopiles either for the direct prediction of pile behaviour or for extracting soil reaction curves which can be incorporated into simplified one-dimensional analyses, if a large number of foundations and load cases must be scrutinised. The appropriate selection of the soil constitutive model and calibration of its parameters are of crucial importance in any numerical analysis and will invariably rely on material characterisation either from in-situ testing or laboratory testing on high-quality, representative, undisturbed or reconstituted soil samples.

The soil stress–strain response is dependent on the imposed stress or strain paths. Current laboratory practice for laterally loaded monopile design typically involves triaxial and direct simple shear testing, following simplified analyses considering that triaxial conditions mimic the loading state of soil elements in front of the laterally loaded pile while simple shear tests reproduce the tangential shearing experienced by elements on the side of the pile (Randolph and Houlsby, 1984; Fan and Long, 2005; Won et al., 2015; Ahmed and Hawlader, 2016; Andersen et al., 2013). However, the stress state of soil surrounding a laterally loaded pile is expected to be more complex and invariably rotation

* Corresponding author.

E-mail addresses: Xiaoyang.Cheng@bristol.ac.uk (X. Cheng), Erdin.Ibraim@bristol.ac.uk (E. Ibraim), haoyuan.liu@ngi.no (H. Liu), F.Pisano@tudelft.nl (F. Pisanò), Andrea.Diambra@bristol.ac.uk (A. Diambra).

<https://doi.org/10.1016/j.compgeo.2022.105139>

Received 6 June 2022; Received in revised form 11 September 2022; Accepted 8 November 2022

0266-352X/© 2022 The Authors. Published by Elsevier Ltd. This is an open access article under the CC BY license (<http://creativecommons.org/licenses/by/4.0/>).

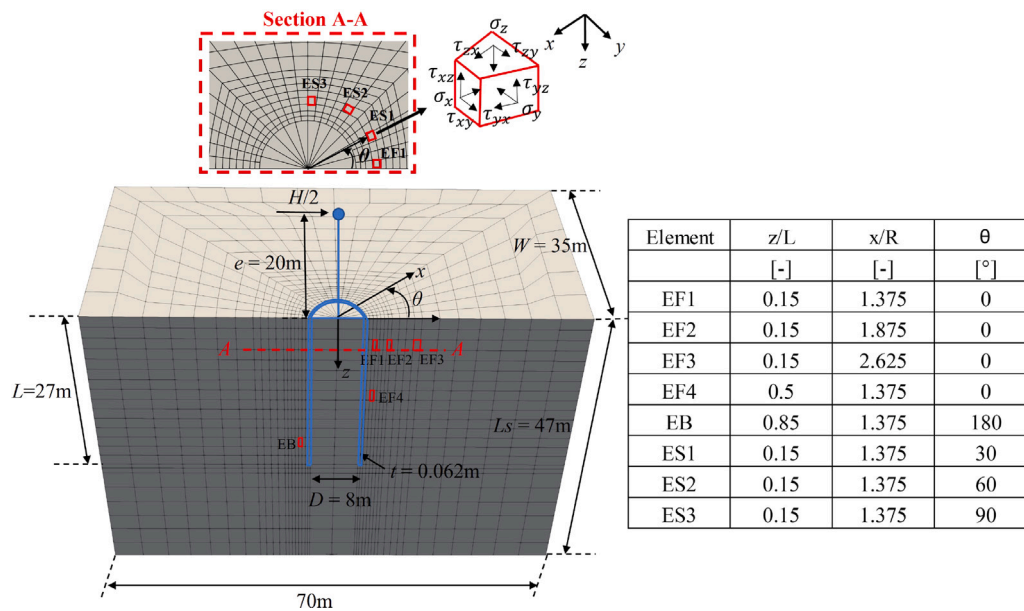


Fig. 1. Finite element model and investigated soil elements.

Table 1
Values of parameters used in the memory surface constitutive model (Liu et al., 2021).

Description	Parameter	Value		
		Karlsruhe sand	Pile-sand interface	
Elasticity	Dimensionless shear modulus	G_0	110	73.3
	Poisson's ratio	ν	0.3	0.3
Critical state	Critical stress ratio in compression	M	1.27	0.953
	Compression to extension strength ratio	c	0.712	0.712
	Reference critical void ratio	e_0	0.845	0.845
	Critical state line shape parameter	λ_c	0.049	0.049
	Critical state line shape parameter	ξ	0.27	0.27
Yield surface	Yield locus opening parameter	m	0.01	0.01
Plastic modulus	Hardening parameter	h_0	5.95	5.95
	Hardening parameter	c_h	1.01	1.01
	Void ratio dependence parameter	n^p	2.0	2.0
	Dilatancy	'Intrinsic' dilatancy parameter	A_0	1.06
	Void ratio dependence parameter	n^d	1.17	1.17

of principal stress axes within the soil around the pile is expected to occur (i.e. Andersen et al. 2013, Yang et al. 2022). Laboratory element studies have shown that soil stiffness degradation and monotonic/cyclic strain development, crucial inputs in monopile design procedures, can be affected by the rotation of principal stress axes (Miura et al. 1986, Wichtmann et al. 2007, Tong et al. 2010, Mandolini et al. 2021, among others).

This research seeks, for the first time, to investigate the stress paths experienced by soil around laterally loaded piles in order to:

- (1) discover the characteristics of the stress paths experienced by representative soil elements;
- (2) assess the relevance of current laboratory testing practices to reproduce the stress paths;
- (3) provide suggestions for replicating these stress paths through laboratory element testing.

The research work employs 3D FE analyses, using implicit constitutive modelling, to assess and extract stress paths in the soil around laterally loaded piles. The work focuses on offshore wind monopile foundations installed in sand under drained monotonic lateral loading conditions. Assessing the monopile behaviour under monotonic conditions invariably forms the first fundamental step of monopile design to identify the backbone monotonic curve on which ultimate limit state and cyclic design procedures build upon.

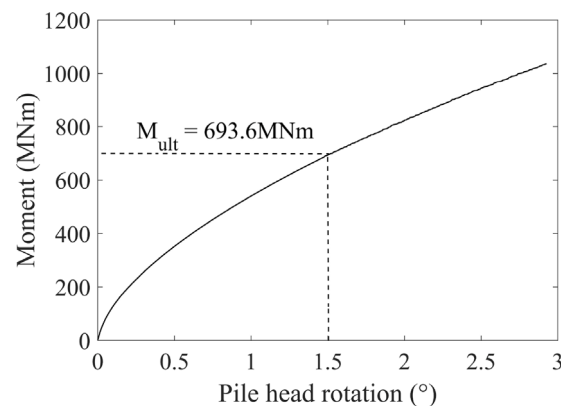


Fig. 2. FE outputs: Moment versus pile head rotation.

2. Reference system and notation

This section introduces the spatial coordinate and stress reference systems used in this investigation. Fig. 1 illustrates the 3D FE model of the reference pile–soil system (half-problem due to plane of symmetry), including the cylindrical coordinate system (x, θ, z) employed for defining the position of the soil elements around the pile, where x axis

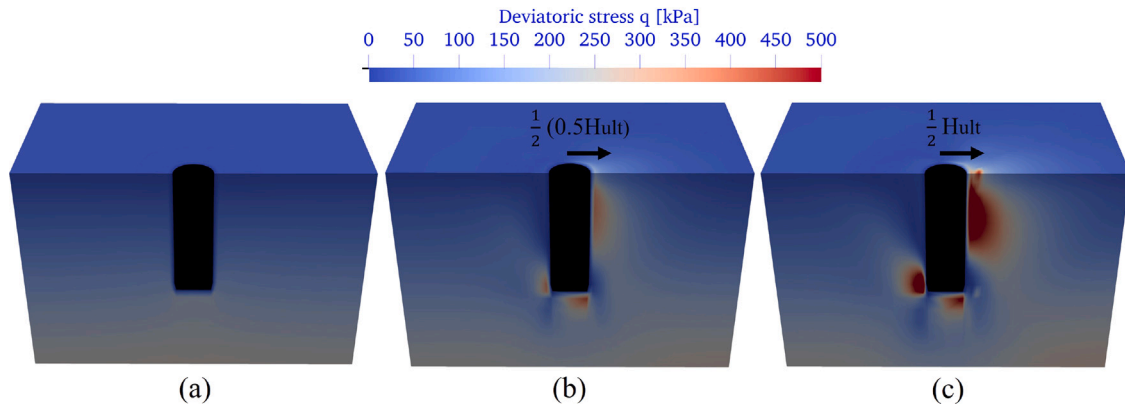


Fig. 3. Contours of deviatoric stress at (a) initial stage (after pile generation), (b) half of ultimate loading condition and (c) ultimate loading condition.

is the radial direction from the pile centre, the z axis is the vertical axis and θ is the angle from the lateral pile loading direction to the element's location. As shown in Fig. 1, the stress state is defined using six stress components ($\sigma_x, \sigma_y, \sigma_z, \tau_{xy}, \tau_{yz}, \tau_{xz}$) in the local coordinate system (x, y, z). Compressive normal stresses are positive. The stress invariants are the mean pressure p , the deviatoric stress q and the Lode's angle θ_L , defined as following:

$$p = \frac{\sigma_x + \sigma_y + \sigma_z}{3} \quad (1)$$

$$q = \left[\frac{(\sigma_x - \sigma_y)^2 + (\sigma_y - \sigma_z)^2 + (\sigma_z - \sigma_x)^2}{2} + 3(\tau_{xy}^2 + \tau_{yz}^2 + \tau_{xz}^2) \right]^{1/2} \quad (2)$$

$$\theta_L = \frac{\arcsin\left(-\frac{3\sqrt{3}}{2} \frac{S}{J^{1.5}}\right)}{3} \quad (3)$$

where

$$S = (\sigma_x - p)(\sigma_y - p)(\sigma_z - p) - (\sigma_x - p)\tau_{yz}^2 - (\sigma_y - p)\tau_{xz}^2 - (\sigma_z - p)\tau_{xy}^2 + \tau_{xy}\tau_{yz}\tau_{xz} \quad (4)$$

$$J = \frac{\sqrt{3}q}{3} \quad (5)$$

θ_L varies between -30° and 30° with $\theta_L = -30^\circ$ corresponding to triaxial compression and $\theta_L = 30^\circ$ to triaxial extension.

3. FE modelling of soil-monopile and overall outputs

3.1. 3D FE modelling configuration

A representative steel hollow monopile foundation of a typical 8 MW capacity wind turbine driven in medium-dense sand (relative density $D_r = 50\%$) has been selected as a case study, based also on data from Kementzetzidis et al. (2019). The dimensions of the monopile foundation, diameter $D = 8.0$ m, embedded length $L = 27.0$ m and wall thickness $t = 0.062$ m, are illustrated in Fig. 1.

The 3D FE model has been built in the Opensees software (McKenna, 1997) following a procedure already adopted and thoroughly tested by Corciulo et al. (2017), Kementzetzidis et al. (2019), Cheng et al. (2021) and Liu et al. (2021). The overall dimensions of the soil domain are $70 \text{ m} \times 35 \text{ m} \times 47 \text{ m}$ to minimise the effect of the boundary conditions on the stress distribution in the soil adjacent to the monopile, as shown in Corciulo et al. (2017) and Liu et al. (2021). The pile is modelled as a linear-elastic 3D hollow cylinder represented by a Young's modulus, $E = 200$ GPa, the unit weight of steel, $\gamma_s = 77$ kN/m³ and Poisson's ratio, $\nu = 0.30$. The above-ground part of the pile is modelled as an elastic beam by using 20 Timoshenko beam elements. The soil-pile interface is simulated according to Griffiths (1985) by inserting a thin layer of solid elements, with a thickness equal to 4% of the monopile diameter along the shaft, 8% of the pile diameter under the pile tip. The elastic shear modulus and critical stress ratio

of these thin layers of solid elements are set to, respectively, 2/3 and 3/4 times lower than those of the surrounding soil, as recommended by Kementzetzidis et al. (2019) to account for the 'friction fatigue' promoted by initial pile driving (Randolph and Gourvenec, 2017).

The soil behaviour has been modelled using the enhanced version of critical state, bounding surface, kinematic hardening SANISAND2004 constitutive model (Dafalias and Manzari, 2004), named SANISAND-MS. The adopted monotonic values of the soil constitutive parameters are the same with those proposed by Liu et al. (2019, 2021) for Karlsruhe sand, as summarised in Table 1. Successful application of the SANISAND-MS model to a 3D FE analysis of a monotonically loaded monopile-soil interaction system was done by Liu et al. (2021). The soil is considered to respond in drained conditions and an effective soil unit weight $\gamma' = 9.4$ kN/m³ was also considered.

The procedure of the numerical analysis has been performed in the following steps:

- (1) Application of soil's self-weight (geostatic pressure);
- (2) Generation of a wished in place monopile. The effects of disturbance of the soil surrounding the monopile are not explicitly considered in this study. However, some considerations of the installation effects on the soil stress paths will be briefly discussed;
- (3) Application of the lateral monotonic load ($H/2$ due to the symmetry of the problem) with an eccentricity (e) of 20 m above ground level (H and e as defined in Fig. 1).

3.2. Overall FE outputs and inspection of soil behaviour

The overall monotonic moment-pile head rotation response of the monopile foundation is reported in Fig. 2. The capability of reproducing the monopile-soil interaction has been validated by Corciulo et al. (2017), Kementzetzidis et al. (2019) and Liu et al. (2021) who used the same 3D FE model with slightly different geometries or soil parameters. An ultimate limit state condition (ULS) corresponding to a 1.5° pile head rotation (an arbitrary value within the typical limits used in monopile design at ULS which varies between 1° and 4° , i.e. LeBlanc et al. 2010) is considered here to define the ultimate pile capacity. Therefore, the stress paths in the soil elements will be analysed up to this load level, which corresponds to an ultimate horizontal load $H_{ult} = 34.08$ MN and a relative pile head displacement of 0.51 m.

The contours in Fig. 3 reveal the development of deviatoric stress (q) around the pile shaft after "wished in place" pile generation (Fig. 3(a)) and during the application of the lateral load at two stages $0.5H_{ult}$ (Fig. 3(b)) and H_{ult} (Fig. 3(c)). Please note that the pile is still modelled as a hollow cylinder and its solid shading is providing only for the sake of clarity. As expected, the most loaded soil sections appear to be arch shape generated in the upper part of the monopile and at the back toe of the pile. As the applied load increases, the extent of the pressure arch

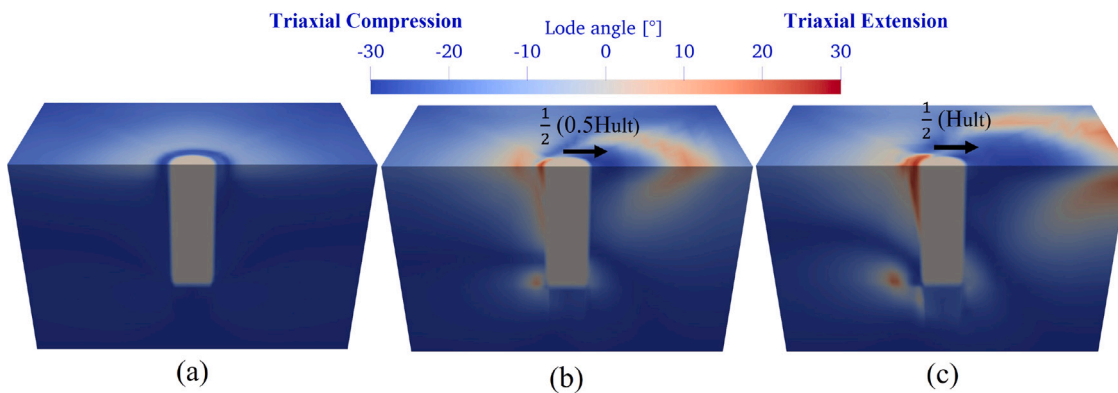


Fig. 4. Contours of Lode's angle at (a) initial stage (after pile generation), (b) half of ultimate loading condition and (c) ultimate loading condition.

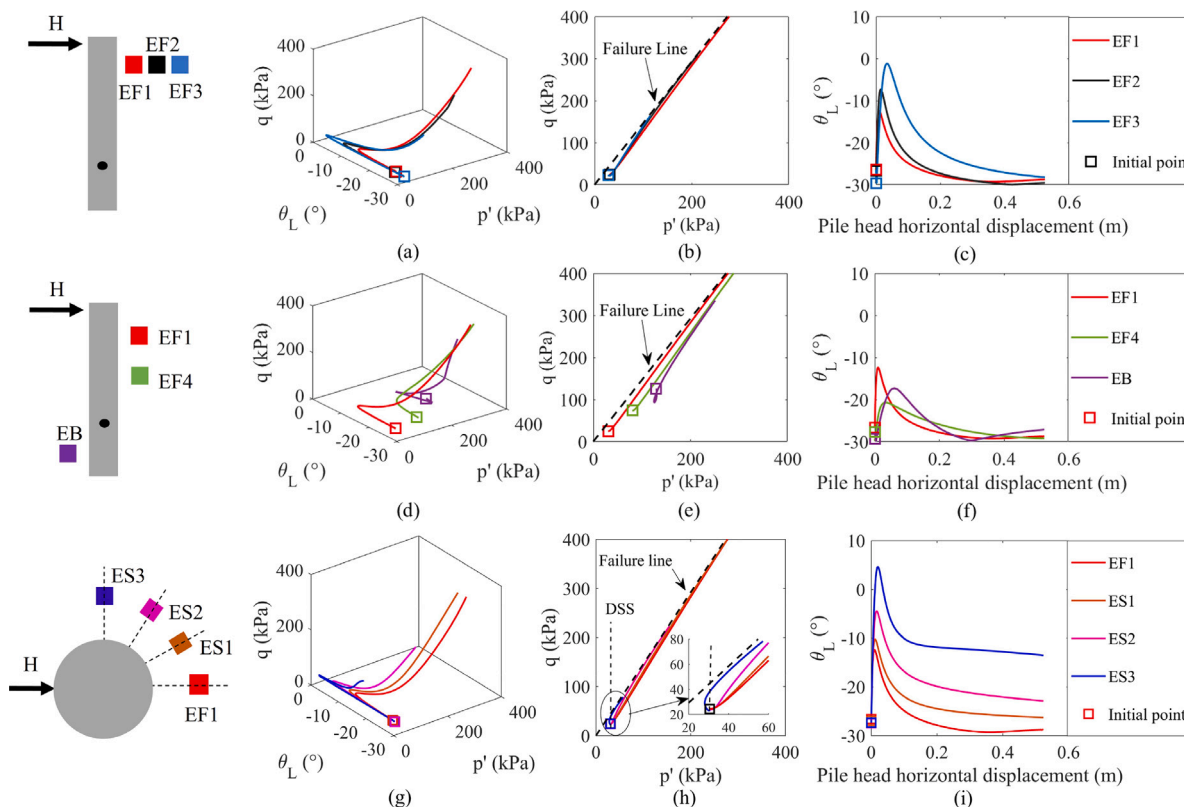


Fig. 5. Stress paths in $p' - q - \theta_L$ space, projection on $p' - q$ plane and relationship between θ_L and pile head horizontal displacement for soil elements at: different distance to pile (a, b, c), different depth below ground level (d, e, f) and different orientation with respect to loading direction (g, h, i). Note that the failure line has been drawn for triaxial compression conditions.

in the surrounding soil also increases. At the ultimate load conditions, the range of the influence of the upper pressure arch in front of the pile reaches to about $2R$ (where R = pile radius) radial distance from the pile shaft and extends over the top three quarters of the pile length.

The 3D spatial distribution of the Lode's angle (θ_L) is shown in Fig. 4. The soil's stress state before the application of lateral loading is largely characterised by $\theta_L = -30^\circ$, which corresponds to triaxial compression (Fig. 4(a)). As the lateral load is applied (Fig. 4(b) shows stress states for 50% ultimate load), the Lode's angle in soil elements in front of the pile shows areas of triaxial compression ($\theta_L = -30^\circ$) transitioning to triaxial extension ($\theta_L = 30^\circ$) further away from the pile. Triaxial extension is also experienced by soil elements, at the back of the pile. As the lateral loading reaches ultimate conditions (Fig. 4(c)), the areas subjected to triaxial compression in front of the pile and to triaxial extension at the back of the pile increase. Such observations

are consistent with those reported in other FE studies of monopile foundations in sand, such as Taborda et al. (2020).

3.3. Analysis of stress invariants

The analysis of the stress invariants is conducted for eight representative soil elements in the vicinity of the laterally loaded pile as shown in Fig. 1. Their location is defined in the table provided within the same figure. The soil elements EF1-4 located in front of the pile (EF1-3 at the same depth) and the EB element, at the back of the pile, are all in-plane with the lateral pile loading direction (Fig. 1). The soil elements ES1-3 are located at the same depth as EF1-3 but off-plane with respect to the lateral loading direction, at different angles θ as defined in Fig. 1.

The overall stress paths experienced by the eight representative samples in terms of the stress invariants $p' - q - \theta_L$ are reported in

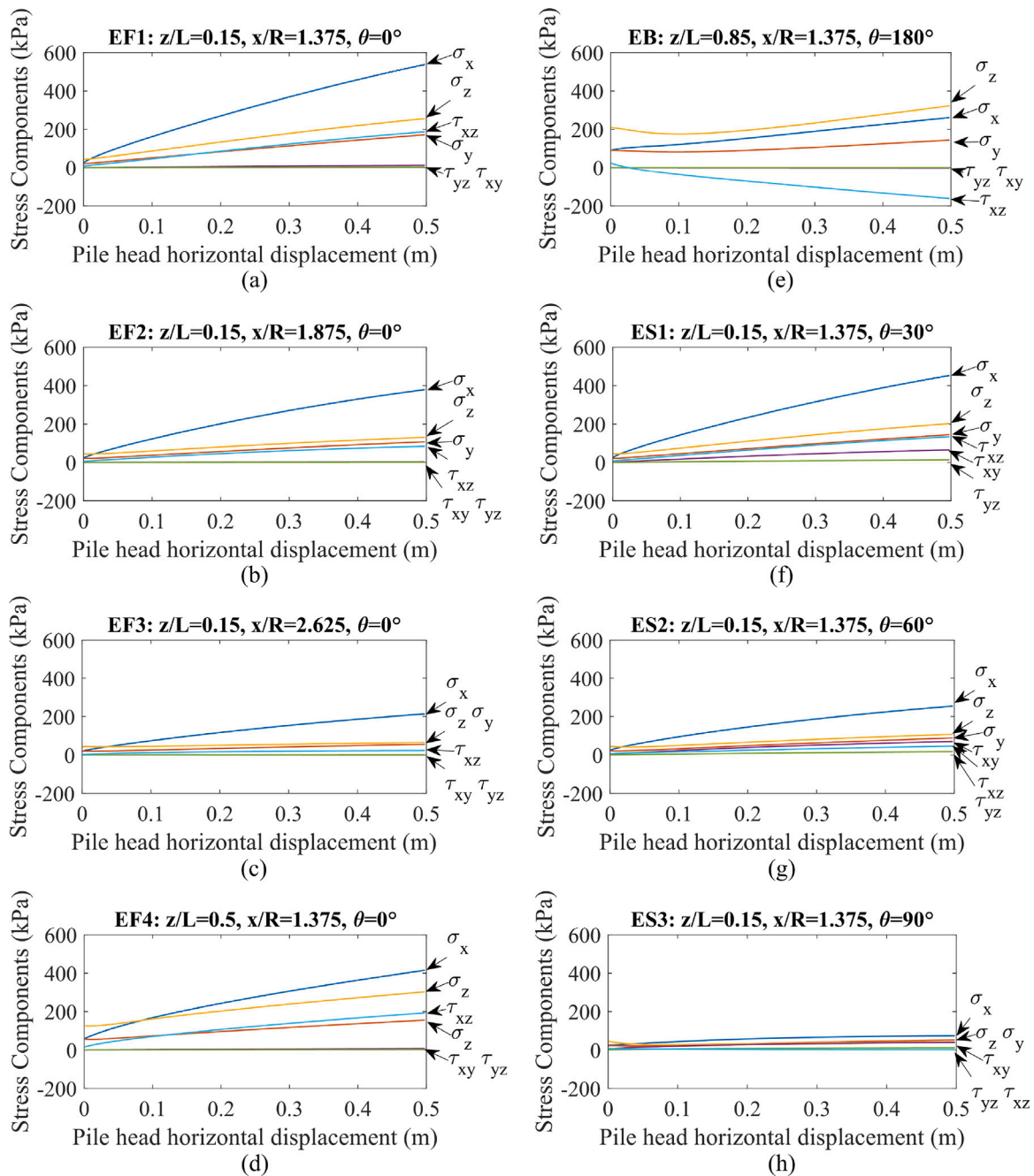


Fig. 6. Stress components in soil elements at various positions: (a) element EF1, (b) element EF2, (c) element EF3, (d) element EF4, (e) element EB, (f) element ES1, (g) element ES2, (h) element ES3.

Fig. 5. The stress paths are grouped in such way they provide the effects of the horizontal distance (Figs. 5(a)–5(c)), depth (Figs. 5(d)–5(f)) and orientation (Figs. 5(g)–5(i)) of the soil elements with respect to the pile. For each group, three dimensional views of the stress paths (Figs. 5(a), 5(d) and 5(g)), their projections on the $p' - q$ plane (Figs. 5(b), 5(e) and 5(h)) and the evolution of the Lode's angle θ_L versus the pile displacement (Figs. 5(c), 5(f) and 5(i)) are reported. All the soil elements undergo shearing under increase of mean effective pressure, which is due to the increase of all normal stress components as shown in Figs. 5(b), 5(e) and 5(h). For all the elements, the Lode's angle θ_L shows a sharp increase from an initial stress condition close to triaxial compression ($\theta_L \sim -25^\circ - 30^\circ$) to reach a peak before a decrease towards an asymptotic value (Figs. 5(c), 5(f) and 5(i)). While the asymptotic value is close to triaxial compression for all the elements at $\theta = 0^\circ$ (Figs. 5(c) and 5(f)), the rate with which the triaxial

condition is reached is reduced as the elements move away from the pile (Fig. 5(c)), which agrees with the observations from Fig. 4. The trends of Fig. 5(i) (for $\theta \geq 0^\circ$) show that the ultimate loading conditions departs from triaxial compression with increasing θ (i.e. as the soil element moves away from the direction of lateral pile loading). Close inspection of all the stress paths reveals that the peak point of the Lode's angle θ_L in Figs. 5(c), 5(f) and 5(i) is associated with the horizontal radial stress (σ_x) becoming the largest normal stress component.

However, while the Lode's angle provides information on the overall loading conditions (i.e. compression, extension or in-between), it does not consider the loading directions with respect to the material axes. Therefore, the full six-dimensional stress state needs to be analysed, as shown in the following section.

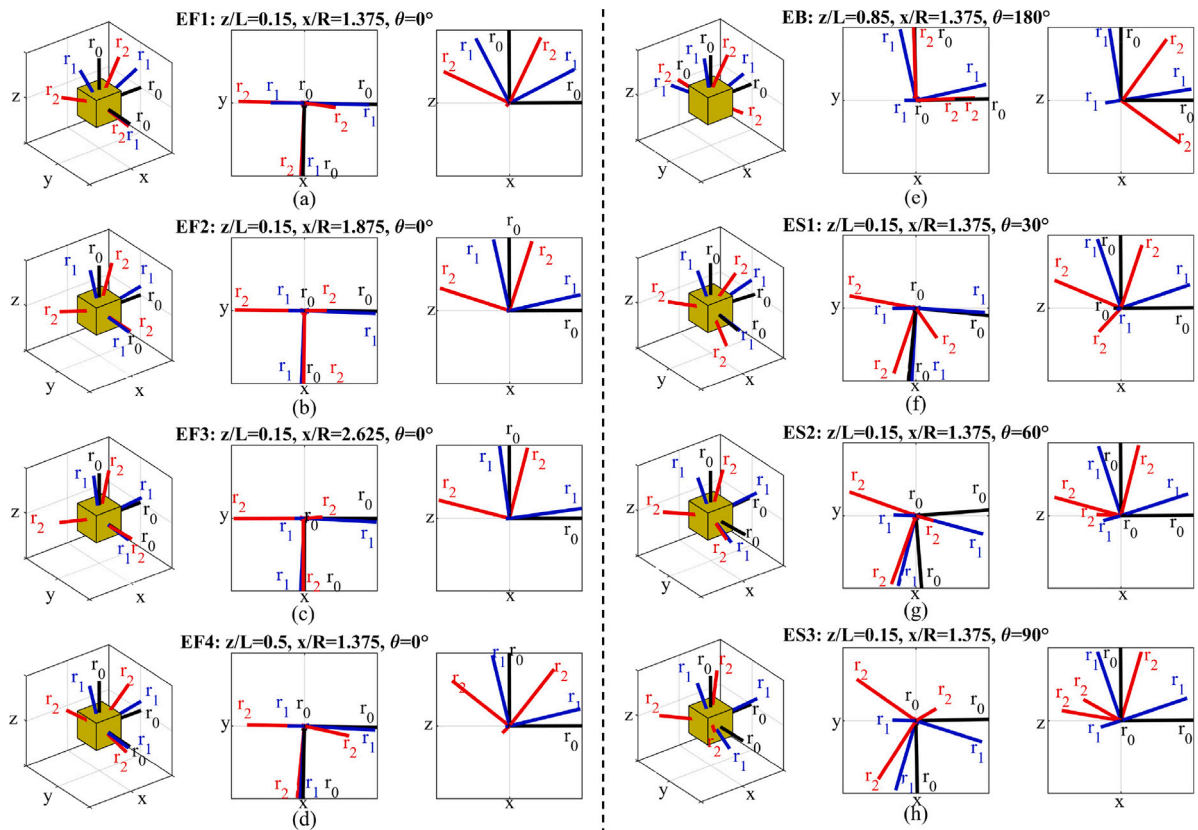


Fig. 7. Rotation of principal stress axis in three-dimensional plots and corresponding projections on $x-z$ plane and $x-y$ plane for elements: (a) element EF1, (b) element EF2, (c) element EF3, (d) element EF4, (e) element EB, (f) element ES1, (g) element ES2, (h) element ES3.

4. Stress variation in soil elements around the pile

4.1. Generalised stress states

The analysis of the six-dimensional stress variation is conducted for the eight representative soil elements (Fig. 1) and illustrated in Fig. 6. For all the elements in-plane with the direction of loading ($\theta = 0^\circ$), elements EF1-4 and EB, the three normal stresses ($\sigma_x, \sigma_z, \sigma_y$) and the shear stress τ_{xz} show significant changes as the horizontal load increases, while the two other components of the shear stress outside the $x-z$ plane (τ_{xy} and τ_{yz}) appear to be negligible (Figs. 6(a)–6(e)).

For the soil elements outside the direction of loading (i.e. $\theta > 0^\circ$, elements ES1-3), the magnitude of variation of all stress components decreases with the increasing of the angle θ . The soil element located orthogonally to the loading direction ($\theta = 90^\circ$, element ES3) developed the lowest changes in all stress components (Fig. 6(h)). It can also be noticed that the shear stress τ_{yz} remains negligible for all the samples with $\theta \neq 0^\circ$ during the whole loading process (Figs. 6(f)–6(h)). Careful inspection of Figs. 6(a) and 6(f)–6(h) confirms the expectation that, as θ increases, the τ_{xz} stress component becomes progressively less influential while the shear stress component τ_{xy} gradually becomes the largest shear stress component.

4.2. Rotation of principal stress axes

Given a specific stress matrix, the determination of eigenvalues and corresponding eigenvectors enables the derivation of the principal stresses and their directions with respect to the original (x, y, z) coordinate system. Therefore, the evolution of the principal stress orientation has been investigated for all the inspected representative soil elements (see Fig. 1) and all trends are reported in Fig. 7. The orientations of the principal stress axes, without distinguishing between major,

intermediate, and minor principal stresses, are represented by unit vectors, r_i , at three stages: (0) initial condition prior to pile generation (r_0 , black vectors), (1) after pile installation (r_1 , blue vectors) and (2) when the lateral load reaches H_{ult} (r_2 , red vectors). Three-dimensional view of the unit vectors orientation as well as their projection on the $x-z$ and $x-y$ planes are also given in Fig. 7. It can be noted that for all the elements aligned with the direction of lateral loading (i.e. $\theta = 0^\circ$) the rotation of principal stress axes takes place in the $x-z$ plane only. For the elements in front of the pile (EF1-4), the rotation of principal stress axes from pile generation to end of loading is between 35° and 70° in the $x-z$ plane. An opposite rotation of principal stress axes for the soil element at the back toe of the pile (element EB), could be noticed compared to the other soil elements, due to the inverse variation of shear stress τ_{xz} . The rotation of the principal stress axis for element EB from pile generation to end of loading is about 45° . As the location of the soil elements moves away from the lateral load direction (increasing θ), the rotation of the principal stress axes in the other two stress planes becomes more pronounced, such that all three principal stress re-orient during loading for elements ES1-3.

4.3. Multiaxial stress paths

The analysis of the multiaxial stress paths is conducted for the lateral pile loading up to H_{ult} . The effects of the radial distance from the pile, depth and orientation with respect to the loading direction of the representative soil elements are taken into consideration.

Effect of radial distance from the pile

The analysis of the variation of the six stress components shown in Fig. 6 revealed that, for all the soil elements in the direction of loading ($\theta = 0^\circ$), the two stress components τ_{xy} and τ_{yz} are negligible.

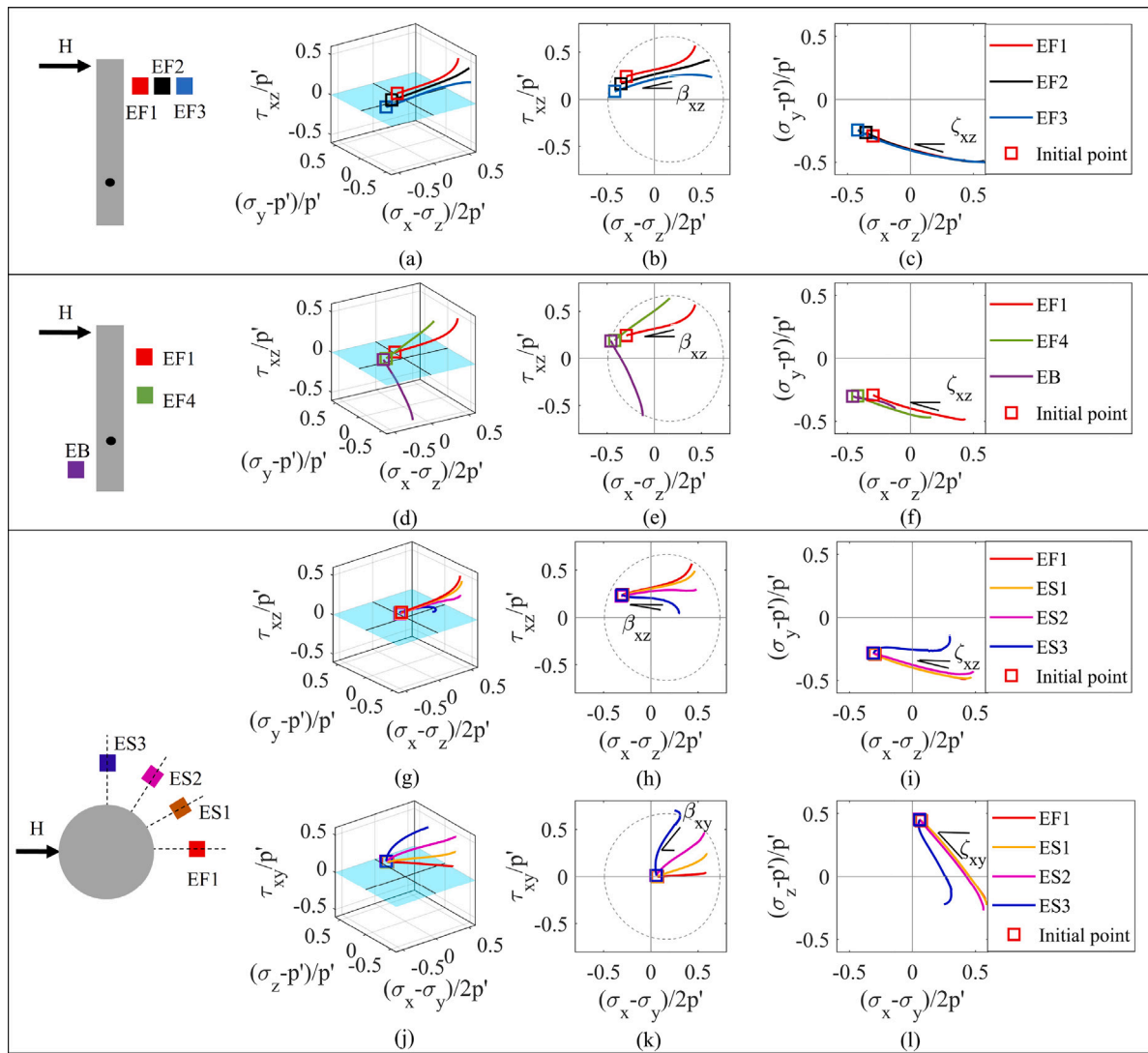


Fig. 8. Stress paths in $(\frac{\tau_{xz}}{p'} \sim \frac{\sigma_x - \sigma_z}{2p'} \sim \frac{\sigma_y - p'}{p'})$ space, projection on $(\frac{\tau_{xz}}{p'} \sim \frac{\sigma_x - \sigma_z}{2p'})$ plane, and on plane $(\frac{\sigma_x - \sigma_z}{2p'} \sim \frac{\sigma_y - p'}{p'})$ for soil elements at: different distance to pile (a, b, c), different depth below ground level (d, e, f) and different orientation with respect to loading direction (g, h, i). Stress paths in $(\frac{\tau_{xy}}{p'} \sim \frac{\sigma_x - \sigma_y}{2p'} \sim \frac{\sigma_z - p'}{p'})$ space, projection on $(\frac{\tau_{xy}}{p'} \sim \frac{\sigma_x - \sigma_y}{2p'})$ plane, and on plane $(\frac{\sigma_x - \sigma_y}{2p'} \sim \frac{\sigma_z - p'}{p'})$ for soil elements at different orientation with respect to loading direction (j, k, l).

Therefore, the evolution of the remaining four stress components is analysed in the three dimensional stress space $(\frac{\tau_{xz}}{p'} \sim \frac{\sigma_x - \sigma_z}{2p'} \sim \frac{\sigma_y - p'}{p'})$, which combines the deviatoric stress plot in the plane $x - z$ ($\frac{\tau_{xz}}{p'} \sim \frac{\sigma_x - \sigma_z}{2p'}$ stress plane) with the addition of the deviatoric stress axis ($\frac{\sigma_y - p'}{p'}$) to consider the influence of the out of plane (intermediate) stress (Wood, 2017), as shown in Fig. 8. The Matsuoka and Nakai (1974) peak failure envelope for the sand material for an assumed friction angle ϕ of 36° is provided for reference in the $(\frac{\tau_{xz}}{p'} \sim \frac{\sigma_x - \sigma_z}{2p'})$ plane (Figs. 8(b), 8(e) and 8(h)). The applicability of the Matsuoka–Nakai criterion for the material tested and the loading conditions was demonstrated by Mandolini et al. (2019).

The three-dimensional stress paths, alongside two planar projections, are presented in Figs. 8(a)–8(c) for all the elements at $\theta = 0^\circ$ and depth $z/L = 0.15$ at different distance in front of the pile (elements EF1–3). The stress paths in $(\frac{\tau_{xz}}{p'} \sim \frac{\sigma_x - \sigma_z}{2p'})$ plane (Fig. 8(b)) follow an almost linear trajectory, whose slope is defined here as $\beta_{xz} = \Delta \frac{\tau_{xz}}{p'} / \Delta \frac{\sigma_x - \sigma_z}{2p'}$. The inclination β_{xz} is rather similar for all considered elements and its numerical values will be analysed in the next section. However, it can be noticed from Fig. 8(b) that the closer the element to the pile, the larger the shear component τ_{xz} becomes.

The projections of the stress paths on the stress plane $(\frac{\sigma_x - \sigma_z}{2p'} \sim \frac{\sigma_y - p'}{p'})$ superimpose (see Fig. 8(c)). They also appear rather linear and could be characterised by a sole inclination ($\zeta_{xz} = \Delta \frac{\sigma_y - p'}{p'} / \Delta \frac{\sigma_x - \sigma_z}{2p'}$) of about -15° (adopted sign convention for angles is positive anticlockwise).

Effect of depth along the pile

The three-dimensional stress paths and their projections for the soil elements located in line with the loading direction but at different depths are reported in Figs. 8(d)–8(f). Fig. 8(d) shows that, while the two elements in front of the pile follow a qualitatively similar stress path, the element EB is subjected to a rather different evolution of the stress state. Fig. 8(e) demonstrates that the difference is mostly related to the stress components of the vertical deviatoric projection plane $(\frac{\tau_{xz}}{p'} \sim \frac{\sigma_x - \sigma_z}{2p'})$ and particularly to the reversed value of the shear stress τ_{xz} as well as to the σ_x stress components not exceeding the magnitude of the σ_z components. The slope β_{xz} for EB soil element is about -60° .

The values of the slope β_{xz} for a larger set of soil elements located at varying distance from the front face of the pile and with soil depth is reported in Fig. 9. The β_{xz} values show limited changes for element locations up to $4.5R$ distance from the pile shaft, then decreases at

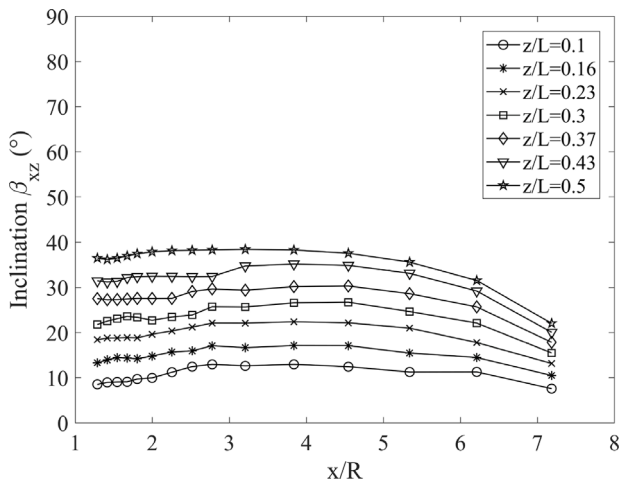


Fig. 9. Relationship between inclination β_{xz} of stress path for element in front of pile and distances at various depth.

further distance from the piles. For soil elements within the top third of the pile, expected to be the most loaded and contribute to the lateral loading soil resistance, β_{xz} values lie in the range of 10° to 25° .

The stress paths projection in Fig. 8(f) are rather coincident and independent whether the element is in front or at the back of the pile. The stress paths are characterised by the same inclination ζ_{xz} of about -15° .

Effect of orientation with respect to the loading direction (same distance from the pile shaft)

It has been shown in Fig. 6 that for the soil elements outside the direction of loading (i.e. $\theta > 0^\circ$, elements ES1-3), the stress state is defined by five stress components, with the component τ_{yz} , being negligible. Therefore the representation of the stress paths for these elements requires two 3D stress spaces: $(\frac{\tau_{xz}}{p'} \sim \frac{\sigma_x - \sigma_z}{2p'} \sim \frac{\sigma_y - p'}{p'})$ and $(\frac{\tau_{xy}}{p'} \sim \frac{\sigma_x - \sigma_y}{2p'} \sim \frac{\sigma_z - p'}{p'})$ as shown in Figs. 8(g) and 8(j) respectively.

The stress paths in the $(\frac{\tau_{xz}}{p'} \sim \frac{\sigma_x - \sigma_z}{2p'} \sim \frac{\sigma_y - p'}{p'})$ space show larger increase of the normalised shear stress component in the $x-z$ plane for low values of θ , while becoming constant for $\theta = 60^\circ$ to then showing a decreasing trend for the element positioned on the side of the pile ($\theta = 90^\circ$). As a result, β_{xz} decreases as θ increases. The projections of the stress paths on the stress plane $(\frac{\sigma_x - \sigma_z}{2p'} \sim \frac{\sigma_y - p'}{p'})$, Fig. 8(i), superimpose and show the same ζ_{xz} inclination as for the other elements in front of the pile except for $\theta = 90^\circ$ which shows $\zeta_{xz} = 0^\circ$.

Conversely, the analysis of the vertical deviatoric projection plane $(\frac{\tau_{xy}}{p'} \sim \frac{\sigma_x - \sigma_y}{2p'})$ stress plane in Fig. 8(k) reveals that all the stress paths start close to the origin and follow a rather linear trajectory with an inclination $(\beta_{xy} = \Delta \frac{\tau_{xy}}{p'} / \Delta \frac{\sigma_x - \sigma_y}{2p'})$ dependent on the element location (θ). Fig. 10(a) shows the variation of β_{xy} for several soil elements around the pile at distance $x/R = 1.375$ but with varying z/L and θ . Evidently, the β_{xy} in Fig. 10(a) shows only little variations from the initial values with the increase of depth. The relationship between β_{xy} and θ is summarised in Fig. 10(b) and it appears that can be reasonably approximated by $\beta_{xy} \approx \theta$.

The projection of the stress paths on the $(\frac{\sigma_x - \sigma_y}{2p'} \sim \frac{\sigma_z - p'}{p'})$ stress plane (Fig. 8(l)) appears also rather linear and could be ideally characterised by an inclination $(\zeta_{xy} = \Delta \frac{\sigma_z - p'}{p'} / \Delta \frac{\sigma_x - \sigma_y}{2p'})$. The projection is rather similar for all the soil elements with a limited variation for ES3. The value of the inclination ζ_{xy} , for all the elements is between -55° and -70° .

5. Relevance of laboratory testing to reproduce the stress paths

This section aims to assess whether available laboratory testing procedures can reproduce field situations (as simulated through 3D FE analysis).

The 3D FE analysis revealed that four stress components vary in magnitude for all the elements in front and back of the pile, whereas a change of five stress components is involved for those soil elements out-of-plane with the lateral loading direction. Given these observations, it is clear that no laboratory apparatus is able to reproduce the prescribed stress paths for soil elements out-of-plane with the lateral loading direction. Concerning the other soil elements, the Hollow Cylinder Torsional Apparatus (HCTA) is the only apparatus that may offer the control of four stresses. However, as a degree of approximation, given the similarity of the stress paths in Fig. 8(g) and the element in line with the direction of loading (i.e. Fig. 8(a)), only the stress paths in the $(\frac{\tau_{xy}}{p'} \sim \frac{\sigma_x - \sigma_y}{2p'} \sim \frac{\sigma_z - p'}{p'})$ space are considered for the soil elements located out of the lateral loading plane as such the HCTA could also be employed for these elements. Nevertheless, when imposing HCTA loading conditions, it will be taken into account the restrictions of the availability of the stress space due to the sample geometry and boundary effects (Hight et al., 1983). Based on the 3D FE analysis, it has also been shown that the stress paths experienced by the soil elements around the pile shaft are fairly linear during monotonic pile loading. Therefore, consideration of linear stress paths in experiments is considered an acceptable approximation.

5.1. Evaluation of laboratory stress paths

The HCTA stress paths, that replicate FE predictions for four representative soil elements in different locations around the laterally loaded pile, are shown in Fig. 11 as follows:

- **CASE F:** soil element in front to the laterally loaded pile, representative element EF1.
- **CASE B:** soil element at the back of the laterally loaded pile, representative element EB.
- **CASE D:** soil element diagonal to the loading direction, representative element ES2.
- **CASE S:** soil element on the side of the laterally loaded pile, representative element ES3

Fig. 11 shows the HCTA admissible stress paths according to the restriction on the applicable ratio of internal (P_i) to external (P_o) pressures to avoid major stress non-uniformities across the sample wall: $0.9 < P_o/P_i < 1.2$ by Hight et al. (1983). The stress paths for simpler triaxial or simple shear conditions are also reported in Fig. 11, where considered appropriate.

Fig. 11 shows that the HCTA can well reproduce the stress paths on the main deviatoric projection plane $(\frac{\tau_{xz}}{p'} \sim \frac{\sigma_x - \sigma_z}{2p'})$ or $(\frac{\tau_{xy}}{p'} \sim \frac{\sigma_x - \sigma_y}{2p'})$ in Figs. 11(b), 11(e), 11(h) and 11(k) but some differences on the location of the stress state at the early loading stage can be noticed in the 3D plots for all the cases (Figs. 11(a), 11(d), 11(g) and 11(j)). This is due to the initial value of the intermediate principal stress as shown in the $(\frac{\sigma_x - \sigma_z}{2p'} \sim \frac{\sigma_y - p'}{p'})$ or $(\frac{\sigma_x - \sigma_y}{2p'} \sim \frac{\sigma_z - p'}{p'})$ projection planes (Figs. 11(c), 11(f), 11(i) and 11(l)). Only higher ratios of P_o/P_i well outside the applicable limits would enable to match the FE predicted stress paths.

Imposing a ratio $P_o/P_i = 1.2$ may help to approach the initial field conditions but the improvement appears limited and probably does not justify the increased testing complexity and risk of strain localisation. Nevertheless, it should also be remembered that the field stress path was determined considering wished-in-place pile generation and K_0 stress conditions. Ashour et al. (1998) suggested the initial horizontal effective stress in triaxial compression test should take as $\sigma_h = K \cdot \sigma_v$, where $K = 1$ due to pile installation effect. The results from the pile penetration experiments carried out by Jardine et al. (2013) show that

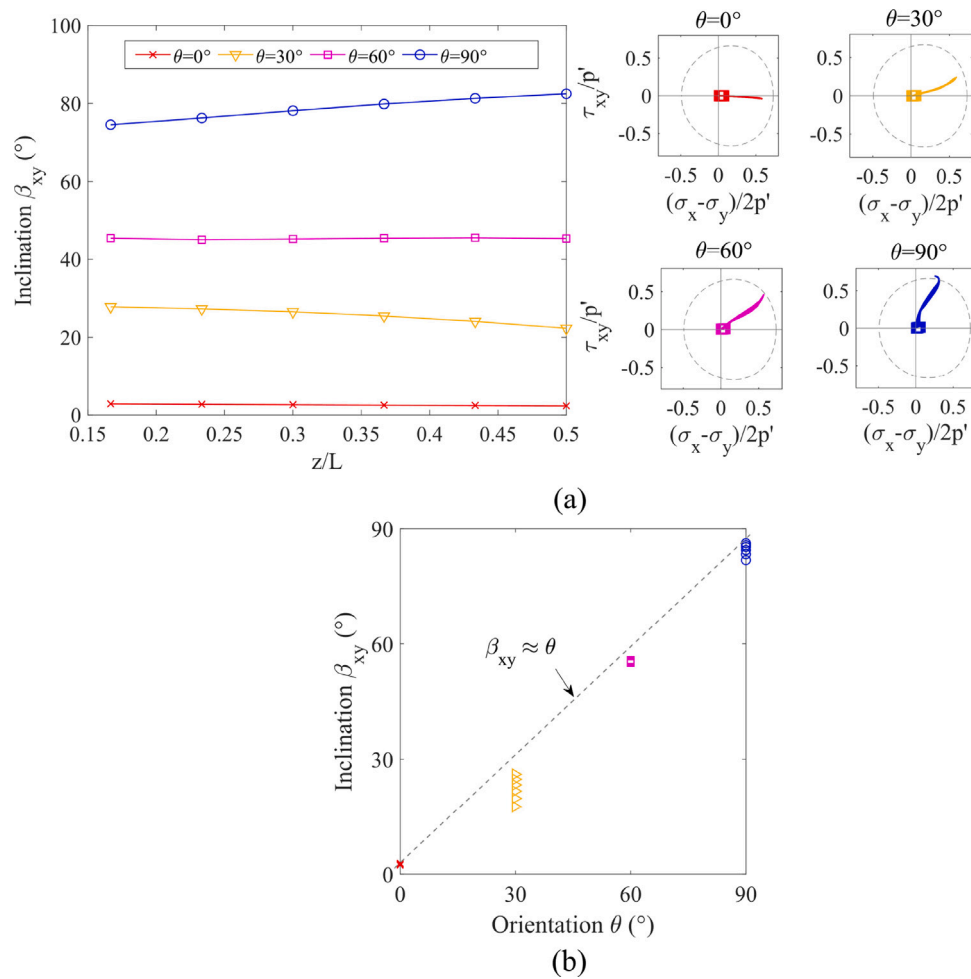


Fig. 10. Variation of β_{xy} for elements at distance $x/R = 1.375$: (a) β_{xy} versus the depth z/L ; (b) relationship between β_{xy} and orientation θ .

horizontal stress is larger than vertical stress for the soil in the vicinity of pile at the end of pile installation. The large increase in magnitude of radial stress after the pile installation was also observed in numerical simulation performed by Staubach et al. (2021). In such conditions, the value of $(\sigma_y - p')$ or $(\sigma_z - p')$ for the initial field stress would approach zero or even change sign, approaching the HCTA stress paths.

Figs. 11(a)–11(c) and 11(d)–11(f) also show that a conventional triaxial test produces a rather different stress path in the multiaxial stress space. Clearly, this type of test cannot reproduce the development of shear stresses due to the frictional pile–soil interaction and the continuous rotation of principal stress axes induced by the lateral loading.

Figs. 11(j)–11(l) show that both HCTA and simple torsional loading (similar to stress condition $P_o = P_i$ in HCTA, which can be associated to simple shear) can reproduce the predicted FE stress path in the $(\frac{\tau_{xy}}{p'} \sim \frac{\sigma_x - \sigma_y}{2p'})$ plane (Fig. 11(k)) at the early loading stage but does not capture the late stage. It is conceivable that a stress path with an orientation β_{xy} slightly lower than 90° may better capture the FE predicted stress path, but the application of a vertical stress path in the $(\frac{\tau_{xy}}{p'} \sim \frac{\sigma_x - \sigma_y}{2p'})$ plane may conversely enable to fully explore the soil behaviour up to pure torsional conditions.

Based on the above discussion, a summary of possible options to reproduce in the laboratory the stress paths of soil elements around monotonic laterally loaded pile is provided in Table 2. The table differentiates among four different soil element locations and provides suggestions for initial and incremental stress conditions to be applied in HCTA testing. The suggested testing conditions match those in the previous section by considering: (1) linearised stress paths; (2) equal

outer and inner cell pressures ($P_o = P_i$); and (3) constant outer and inner cell pressures during shearing, which neglects the large increase in mean isotropic stress observed in Fig. 5 (and whose effect has been normalised throughout the paper), but this follows conventional practice in laboratory exploration of the shear behaviour of soils (i.e. triaxial shear tests are typically performed by maintaining constant cell pressure). Table 2 provides a schematic view of the stress paths in the main deviatoric stress plane only, since the account of the intermediate stress axis is fixed by the condition $P_o = P_i$.

5.2. Note on rotation of stress coordinates between field and laboratory

Laboratory samples are typically obtained from vertical cylindrical cores (in cohesive soils) or prepared through vertical depositional and compaction procedures. During the mechanical testing in the HCTA (or triaxial, simple shear testing), the major variations are applied to the normal or shear stress to a horizontal face.

Therefore, unless special and unconventional sampling or sample preparation procedures are adopted (i.e. horizontal coring from block samples of clays or frozen sands, or laboratory reconstitution/preparation of cylindrical samples maintaining the axis of symmetry horizontal), the orientation between the stress direction and the material axis cannot be maintained between field and laboratory conditions. A relative 90° rotation between the material axis and the stress direction must be applied, as shown in Fig. 12. This denotes one of the limitations of laboratory element testing in soils for laterally loaded piles.

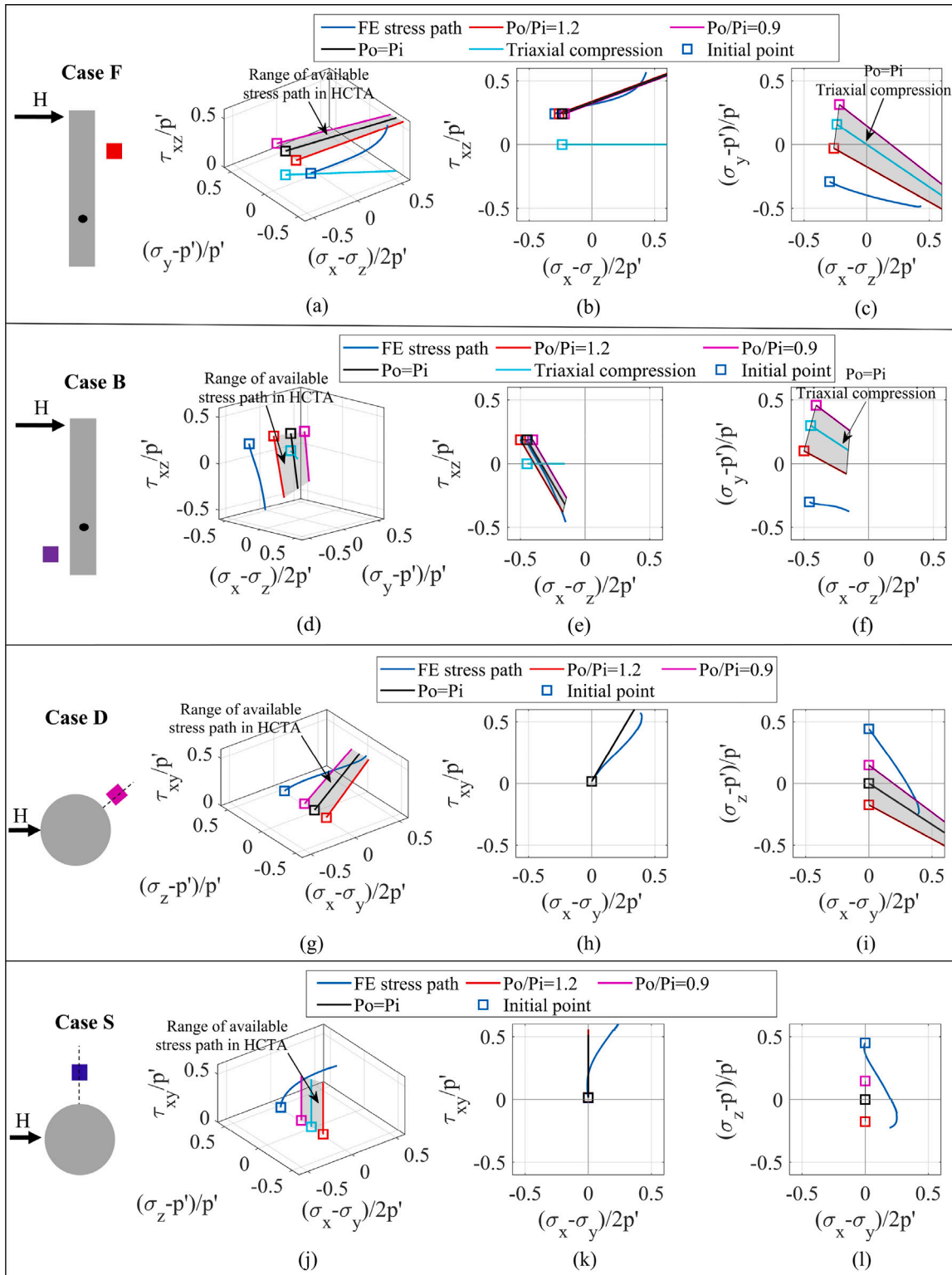
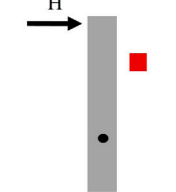
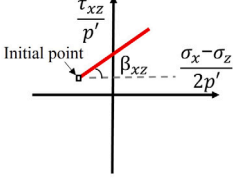
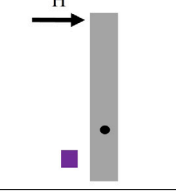
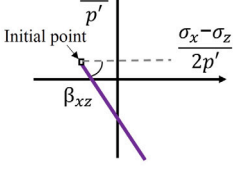
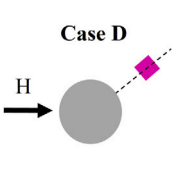
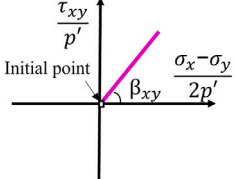
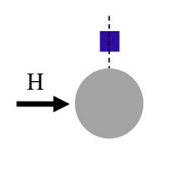
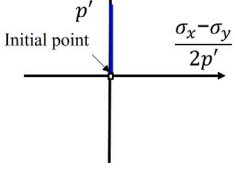


Fig. 11. Comparison between idealised stress paths and those applicable in element testing in $(\frac{\tau_{xz}}{p'} \sim \frac{\sigma_x - \sigma_z}{2p'} \sim \frac{\sigma_y - p'}{p'})$ space, projection on $(\frac{\tau_{xz}}{p'} \sim \frac{\sigma_x - \sigma_z}{2p'})$ plane, and on plane $(\frac{\sigma_y - p'}{p'} \sim \frac{\sigma_x - \sigma_z}{2p'})$ for soil elements Case F (a, b, c), Case B (d, e, f), and in $(\frac{\tau_{xy}}{p'} \sim \frac{\sigma_x - \sigma_y}{2p'} \sim \frac{\sigma_z - p'}{p'})$ space, projection on $(\frac{\tau_{xy}}{p'} \sim \frac{\sigma_x - \sigma_y}{2p'})$ plane, and on plane $(\frac{\sigma_z - p'}{p'} \sim \frac{\sigma_x - \sigma_y}{2p'})$ for soil elements Case D (g, h, i), and Case S (j, k, l).

Table 2
Summary of recommended experimental tests for the soil elements around the laterally loaded pile.

Soil element position	Suggested HCTA testing	
<p>Case F</p> 		<p>Initial conditions:</p> <ul style="list-style-type: none"> • $\sigma_{z0} = \gamma' \cdot z$; • $\sigma_{x0} = \sigma_{y0} = K \cdot \sigma_{z0}$ [K defined to consider pile installation effect]; • $0 \leq \tau_{xz} \leq \sigma_{x0} \cdot \tan(\phi_{ps})$. <p>Incremental stress or strain conditions:</p> <ul style="list-style-type: none"> • Apply vertical stress ($\Delta\sigma_x$) or strain ($\Delta\epsilon_x$) increments; • $\Delta\sigma_z = \Delta\sigma_y = 0$ [constant inner and outer cell pressures]; • $\Delta\tau_{xz} = \frac{\Delta\sigma_x - \Delta\sigma_z}{2} \cdot \tan(\beta_{xz})$. [$\beta_{xz} = 10^\circ$ to 25°]
<p>Case B</p> 		<p>Initial conditions:</p> <ul style="list-style-type: none"> • $\sigma_{z0} = \gamma' \cdot z$; • $\sigma_{x0} = \sigma_{y0} = K \cdot \sigma_{z0}$ [K defined to consider pile installation effect]; • $0 \leq \tau_{xz} \leq \sigma_{x0} \cdot \tan(\phi_{ps})$. <p>Incremental stress or strain conditions:</p> <ul style="list-style-type: none"> • Apply vertical stress ($\Delta\sigma_x$) or strain ($\Delta\epsilon_x$) increments; • $\Delta\sigma_z = \Delta\sigma_y = 0$; [constant inner and outer cell pressures] • $\Delta\tau_{xz} = \frac{\Delta\sigma_x - \Delta\sigma_z}{2} \cdot \tan(\beta_{xz})$. [$\beta_{xz} = -60^\circ$]
<p>Case D</p> 		<p>Initial conditions:</p> <ul style="list-style-type: none"> • $\sigma_{z0} = \gamma' \cdot z$; • $\sigma_{x0} = \sigma_{y0} = K \cdot \sigma_{z0}$ [K defined to consider pile installation effect]; • $\tau_{xy} = 0$. <p>Incremental stress or strain conditions:</p> <ul style="list-style-type: none"> • Apply vertical stress ($\Delta\sigma_x$) or strain ($\Delta\epsilon_x$) increments ($\theta < 45^\circ$); shear stress ($\Delta\tau_{xy}$) or strain ($\Delta\gamma_{xy}$) increments ($45^\circ < \theta < 90^\circ$); • $\Delta\sigma_z = \Delta\sigma_y = 0$; [constant inner and outer cell pressures] • $\Delta\tau_{xy} = \frac{\Delta\sigma_x - \Delta\sigma_z}{2} \cdot \tan(\beta_{xy})$. [$\beta_{xy} \approx \theta$]
<p>Case S</p> 		<p>Initial conditions:</p> <ul style="list-style-type: none"> • $\sigma_{z0} = \gamma' \cdot z$; • $\sigma_{x0} = \sigma_{y0} = K \cdot \sigma_{z0}$ [K defined to consider pile installation effect]; • $\tau_{xy} = 0$. <p>Incremental stress or strain conditions:</p> <ul style="list-style-type: none"> • Apply shear stress ($\Delta\tau_{xy}$) or strain ($\Delta\gamma_{xy}$) increments; • $\Delta\sigma_x = 0$; • $\Delta\sigma_z = \Delta\sigma_y = 0$. [constant inner and outer cell pressures]

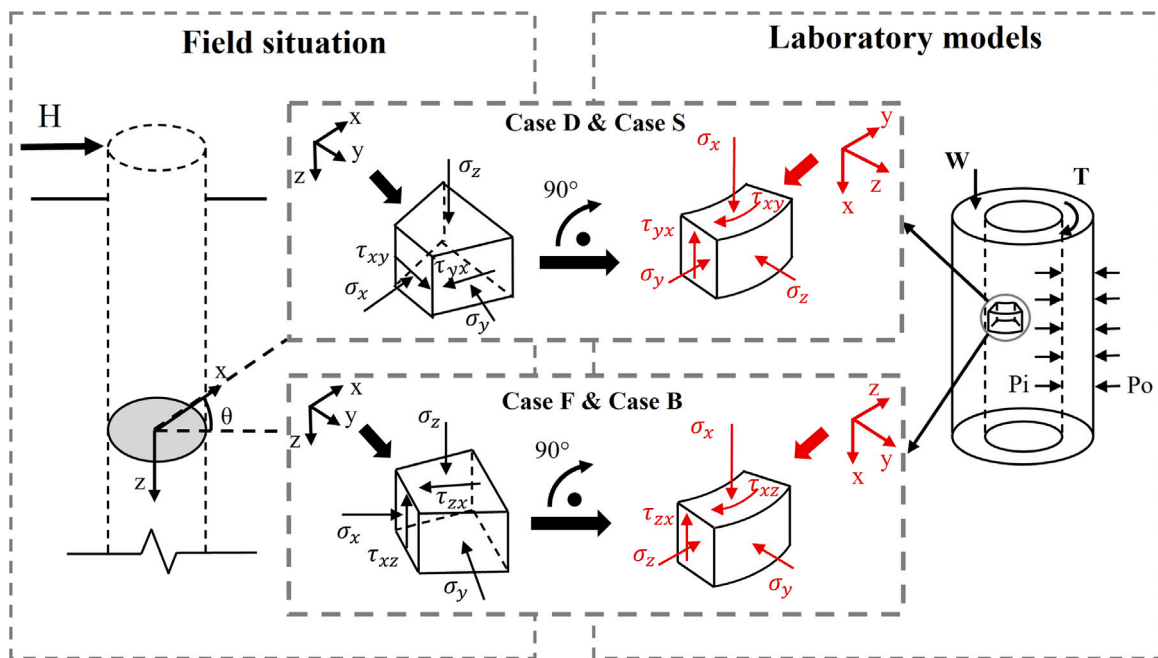


Fig. 12. Schematic of transition from stress state in field situation to that in the HCTA.

6. Summary and conclusions

Using three-dimensional finite element analyses, this paper has investigated the stress paths experienced by soil elements around the monotonically laterally loaded large-diameter pile in granular soils. The main aim of the paper was to determine typical stress paths for soil elements at different locations around the pile and assess whether laboratory element testing procedure can mimic those stress paths and identify the main shortcoming.

Inspection of the full six-dimensional stress state for the selected soil elements demonstrated that either four or five stress components undergo consistent variation as the pile is laterally loaded, inducing variation of Lode's angle and re-orientation of principal stress axes for these soil elements. While there is no experimental apparatus which enables to replicate the full six-dimensional stress state of soil elements around laterally loaded piles, the HCTA is the only laboratory testing equipment which permits the control of orientation and rotation of the principal stress axes. However, if a reduction of the stress-state to four dimensions by neglecting one of the shear stress component for the soil elements out-of-plane of lateral loading is applied, the HCTA could offer a reasonable replication of the numerically determined stress paths.

Typical linearised stress conditions for representative soil elements – front (top) and back (bottom) of the pile in plane with the loading direction as well as diagonal and on the side of the pile – have been determined and they are summarised in Table 2 of this paper alongside the conditions to be applied in HCTA element testing for their simulation. The analysis also identified two further crucial points for further considerations when assessing the relevance of laboratory element testing:

- (1) it appears that the HCTA would be unable to replicate the initial magnitude of the intermediate principal stress from FE predictions, but this limitation may be overruled or alleviated if the pile installation effects are considered;
- (2) there are difficulties in maintaining the relative orientation between material axis and the principal stress direction unless special and unconventional sampling or sample preparation procedures are adopted (i.e. horizontal coring from block samples of clays or frozen sands, or laboratory reconstitution/preparation of cylindrical samples maintaining the axis of symmetry horizontal). Nevertheless, this limitation applies to all laboratory testing equipment and may be critical when dealing with strongly anisotropic geomaterials.

It should be highlighted that the employment of HCTA testing is not seen as a replacement of the current conventional day-to-day testing practice (based on triaxial and direct shear testing) because of the complexity around sample preparation and testing, and the cost/time implications. Nevertheless, it is of utmost importance to recognise the limitations of the current testing practice, which can then be accounted to optimise the current design procedures. Research work using HCTA and exploring the soil behaviour under the proposed stress paths could reveal these shortcomings. In addition, given the nature of the actions in offshore wind applications, the study of the stress paths should be extended to cyclic loadings and further research is ongoing.

CRedit authorship contribution statement

Xiaoyang Cheng: Conceptualization, Methodology, Software, Validation, Formal analysis, Investigation, Data curation, Writing – Original draft, Writing – review & editing. **Erdin Ibrahim:** Conceptualization, Writing – review & editing, Supervision, Project administration. **Haoyuan Liu:** Writing – review & editing. **Federico Pisanò:** Writing – review & editing. **Andrea Diambra:** Conceptualization, Methodology, Validation, Writing – review & editing, Supervision, Project administration.

Declaration of competing interest

The authors declare that they have no known competing financial interests or personal relationships that could have appeared to influence the work reported in this paper.

Data availability

The authors do not have permission to share data.

Acknowledgements

The authors would like to acknowledge the financial support of the first author from China Scholarship Council (CSC) and University of Bristol, UK (CSC201806220008).

References

- Ahmed, S.S., Hawlader, B., 2016. Numerical analysis of large-diameter monopiles in dense sand supporting offshore wind turbines. *Int. J. Geomech.* 16 (5), 04016018. [http://dx.doi.org/10.1061/\(ASCE\)GM.1943-5622.0000633](http://dx.doi.org/10.1061/(ASCE)GM.1943-5622.0000633).
- Andersen, K., Puech, A., Jardine, R., 2013. Cyclic resistant geotechnical design and parameter selection for offshore engineering and other applications. In: *Design for Cyclic Loading: Piles and Other Foundations*, Proceedings of the TC-209 Workshop, Paris, France. Vol. 4. pp. 9–44, URL: https://www.issmge.org/filemanager/technical_committees/20/Worshop_TC_209_at_18th_ICSMGE_-_Design_for_cyclic_loading_-_piles_and_other_foundations.pdf.
- Ashour, M., Norris, G., Pilling, P., 1998. Lateral loading of a pile in layered soil using the strain wedge model. *J. Geotech. Geoenviron. Eng.* 124 (4), 303–315. [http://dx.doi.org/10.1061/\(ASCE\)1090-0241\(1998\)124:4\(303\)](http://dx.doi.org/10.1061/(ASCE)1090-0241(1998)124:4(303)).
- Cheng, X., Diambra, A., Ibrahim, E., Liu, H., Pisanò, F., 2021. 3D FE-informed laboratory soil testing for the design of offshore wind turbine monopiles. *J. Mar. Sci. Eng.* 9 (1), 101. <http://dx.doi.org/10.3390/jmse9010101>.
- Corciulo, S., Zanolli, O., Pisanò, F., 2017. Transient response of offshore wind turbines on monopiles in sand: role of cyclic hydro-mechanical soil behaviour. *Comput. Geotech.* 83, 221–238. <http://dx.doi.org/10.1016/j.compgeo.2016.11.010>.
- Dafalias, Y.F., Manzari, M.T., 2004. Simple plasticity sand model accounting for fabric change effects. *J. Eng. Mech.* 130 (6), 622–634. [http://dx.doi.org/10.1061/\(ASCE\)0733-9399\(2004\)130:6\(622\)](http://dx.doi.org/10.1061/(ASCE)0733-9399(2004)130:6(622)).
- Fan, C.-C., Long, J.H., 2005. Assessment of existing methods for predicting soil response of laterally loaded piles in sand. *Comput. Geotech.* 32 (4), 274–289. <http://dx.doi.org/10.1016/j.compgeo.2005.02.004>.
- Griffiths, D., 1985. Numerical modelling of interfaces using conventional finite elements. URL: http://inside.mines.edu/~vgriffit/pubs/Some_C_Pubs/Nagoya_1985.pdf.
- Hight, D., Gens, A., Symes, M., 1983. The development of a new hollow cylinder apparatus for investigating the effects of principal stress rotation in soils. *Geotechnique* 33 (4), 355–383. <http://dx.doi.org/10.1680/geot.1983.33.4.355>.
- Jardine, R., Zhu, B., Foray, P., Yang, Z., 2013. Measurement of stresses around closed-ended displacement piles in sand. *Géotechnique* 63 (1), 1–17. <http://dx.doi.org/10.1680/geot.9.P.137>.
- Kementzetzidis, E., Corciulo, S., Versteijlen, W.G., Pisanò, F., 2019. Geotechnical aspects of offshore wind turbine dynamics from 3D non-linear soil-structure simulations. *Soil Dyn. Earthq. Eng.* 120, 181–199. <http://dx.doi.org/10.1016/j.soildyn.2019.01.037>.
- LeBlanc, C., Houlsby, G., Byrne, B., 2010. Response of stiff piles in sand to long-term cyclic lateral loading. *Géotechnique* 60 (2), 79–90. <http://dx.doi.org/10.1680/geot.7.00196>.
- Liu, H.Y., Abell, J.A., Diambra, A., Pisanò, F., 2019. Modelling the cyclic ratcheting of sands through memory-enhanced bounding surface plasticity. *Géotechnique* 69 (9), 783–800. <http://dx.doi.org/10.1680/jgeot.17.P.307>.
- Liu, H., Kementzetzidis, E., Abell, J.A., Pisanò, F., 2021. From cyclic sand ratcheting to tilt accumulation of offshore monopiles: 3D FE modelling using SANISAND-MS. *Géotechnique* 1–16. <http://dx.doi.org/10.1680/jgeot.20.P.029>.
- Mandolini, A., Diambra, A., Ibrahim, E., 2019. Strength anisotropy of fibre-reinforced sands under multiaxial loading. *Géotechnique* 69 (3), 203–216. <http://dx.doi.org/10.1680/jgeot.17.P.102>.
- Mandolini, A., Diambra, A., Ibrahim, E., 2021. Stiffness of granular soils under long-term multiaxial cyclic loading. *Géotechnique* 71 (9), 795–811. <http://dx.doi.org/10.1680/jgeot.19.TI.018>.
- Matsuoka, H., Nakai, T., 1974. Stress-deformation and strength characteristics of soil under three different principal stresses. In: *Proceedings of the Japan Society of Civil Engineers*. Vol. 1974. (232), Japan Society of Civil Engineers, pp. 59–70. <http://dx.doi.org/10.2208/jscej1969.1974.232.59>.

- McKenna, F.T., 1997. Object-Oriented Finite Element Programming: Frameworks for Analysis, Algorithms and Parallel Computing. University of California, Berkeley, URL: <https://www.proquest.com/docview/304341094?pq-origsite=gscholar&fromopenview=true>.
- Miura, K., Miura, S., Toki, S., 1986. Deformation behavior of anisotropic dense sand under principal stress axes rotation. *Soils Found.* 26 (1), 36–52. <http://dx.doi.org/10.3208/sandf1972.26.36>.
- Ramirez, L., Fraile, D., Brindley, G., 2020. Offshore wind in Europe: Key trends and statistics 2019. URL: <https://windeurope.org/wp-content/uploads/files/about-wind/statistics/WindEurope-Annual-Offshore-Statistics-2019.pdf>.
- Randolph, M., Gourvenec, S., 2017. *Offshore Geotechnical Engineering*. CRC Press, URL: <https://www.taylorfrancis.com/books/mono/10.1201/9781315272474/offshore-geotechnical-engineering-white-david-cassidy-mark>.
- Randolph, M.F., Houlsby, G., 1984. The limiting pressure on a circular pile loaded laterally in cohesive soil. *Geotechnique* 34 (4), 613–623. <http://dx.doi.org/10.1680/geot.1984.34.4.613>.
- Staubach, P., Macháček, J., Wichtmann, T., 2021. Large-deformation analysis of pile installation with subsequent lateral loading: Sanisand vs. Hypoplasticity. *Soil Dyn. Earthq. Eng.* 151, 106964. <http://dx.doi.org/10.1016/j.soildyn.2021.106964>.
- Taborda, D.M., Zdravković, L., Potts, D.M., Burd, H.J., Byrne, B.W., Gavin, K.G., Houlsby, G.T., Jardine, R.J., Liu, T., Martin, C.M., et al., 2020. Finite-element modelling of laterally loaded piles in a dense marine sand at Dunkirk. *Géotechnique* 70 (11), 1014–1029. <http://dx.doi.org/10.1680/jgeot.18.PISA.006>.
- Tong, Z.-X., Zhang, J.-M., Yu, Y.-L., Zhang, G., 2010. Drained deformation behavior of anisotropic sands during cyclic rotation of principal stress axes. *J. Geotech. Geoenviron. Eng.* 136 (11), 1509–1518. [http://dx.doi.org/10.1061/\(ASCE\)GT.1943-5606.0000378](http://dx.doi.org/10.1061/(ASCE)GT.1943-5606.0000378).
- Wichtmann, T., Niemunis, A., Triantafyllidis, T., 2007. On the influence of the polarization and the shape of the strain loop on strain accumulation in sand under high-cyclic loading. *Soil Dyn. Earthq. Eng.* 27 (1), 14–28. <http://dx.doi.org/10.1016/j.soildyn.2006.05.002>.
- Won, J., Suroor, H., Jang, S., Seo, H., 2015. Strain ϵ^* and stiffness ratio (E^* sub 50°/S^u) for Gulf of Mexico clays. In: *Frontiers in Offshore Geotechnics III: Proceedings of the 3rd International Symposium on Frontiers in Offshore Geotechnics*. Vol. 1. ISFOG 2015, Taylor & Francis Books Ltd, pp. 1121–1126, URL: <https://www.proquest.com/openview/1b82dcf33044f03d661ffae04a0911b/1?pq-origsite=gscholar&cbl=2069209>.
- Wood, D.M., 2017. *Geotechnical Modelling*. CRC Press, URL: <https://www.taylorfrancis.com/books/mono/10.1201/9781315273556/geotechnical-modelling-david-muir-wood>.
- Yang, Y., Sun, Y., Xu, C., Iqbal, K., Xiuli, D., 2022. Predicting accumulated deformation of offshore large-diameter monopile using hollow cylinder apparatus. *Ocean Eng.* 261, 111984. <http://dx.doi.org/10.1016/j.oceaneng.2022.111984>.